Optical Nonlinearity in Silicon Nanowires Enabled by Bound States in the Continuum

Jin-Sung Park[†], *Chentao Li*[§], *Kyoung-Ho Kim*[‖], *Yuankai Tang*[§], *Corban G. E. Murphey*[†], *Taylor S. Teitsworth*[†], *Seokhyoung Kim*[⊥], *Hayk Harutyunyan*[*,§], *and James F. Cahoon*[*,†]

[†]Department of Chemistry, University of North Carolina at Chapel Hill, Chapel Hill, North Carolina 27599, United States

[§]Department of Physics, Emory University, Atlanta, Georgia 30322, United States

[‖]Department of Physics, Chungbuk National University, Cheongju 28644, Republic of Korea

[⊥]Department of Chemistry, Michigan State University, East Lansing, Michigan 48824, United States

ABSTRACT

Intense electromagnetic fields localized within resonant photonic nanostructures provide versatile opportunities for engineering nonlinear optical effects at a subwavelength scale. For dielectric structures, optical bound states in the continuum (BICs)—resonant non-radiative modes that exist within the radiation continuum—are an emerging strategy to localize and intensify fields. Here, we report efficient second and third harmonic generation from Si nanowires (NWs) encoded with BIC and *quasi*-BIC resonances. *In situ* dopant modulation during vapor-liquid-solid NW growth was followed by wet-chemical etching to periodically modulate the diameter of Si NWs and create cylindrically symmetric geometric superlattices (GSLs) with precisely defined axial and radial dimensions. By varying the GSL structure, BIC and *quasi*-BIC resonant conditions were created to span visible and near-infrared optical frequencies. To probe the optical non-linearity of these structures, we collected linear extinction spectra and non-linear spectra from single-NW GSLs, demonstrating that *quasi*-BIC spectral positions at the fundamental frequency are directly correlated with enhanced harmonic generation at second and third harmonic frequencies. Interestingly, we find that deliberate geometric detuning from the BIC condition leads to a *quasi*-BIC resonance with maximal harmonic generation efficiency by providing a balance between the capacity to trap light and couple to the external radiation continuum. Moreover, under focused illumination, as few as 30 geometric unit cells are required to achieve more than 90% of the approximate maximum theoretical efficiency of an infinite structure, indicating that nanostructures with projected areas smaller than ~10 μm^2 can support *quasi*-BICs for efficient harmonic generation. The results represent an important step toward the design of efficient harmonic generation at the nanoscale and further highlight the photonic utility of BICs at optical frequencies in ultracompact one-dimensional nanostructures.

KEYWORDS. nanophotonics, silicon nanowire, nanowire geometric superlattice, bound states in the continuum, nonlinear optics, harmonic generation

INTRODUCTION

Boosting nonlinear optical effects at the nanoscale has been a long-standing interest for photonics because optical nonlinearities are inherently weak and the phase matching condition[1] cannot readily be achievable in subwavelength and wavelength-scale photonic structures.[2-5] One successful strategy is to utilize strong local electromagnetic field confinement of the incident fundamental radiation. For example, metallic and metal–dielectric nanostructures supporting plasmonic resonances can provide electromagnetic field localization and amplitude enhancements, thereby boosting nonlinear optical effects.[2,6-9] However, metallic nanostructures suffer from high dissipative losses, heating, and low damage thresholds. For instance, under high intensity light, the metallic components easily deform by the induced heat, limiting their conversion efficiencies and practical applications.[2,10-12] Therefore, dielectric nanostructures with high refractive indices, low material losses, strong nonlinear susceptibilities, and a range of resonance types[3,5] have emerged as a promising platform for high conversion efficiencies.[13-20]

Recently, exceptionally high quality factor (Q factor) resonances were demonstrated with optical bound states in the continuum (BICs), which are resonant modes within the radiation continuum that originate from destructive interference toward radiation in the far field.[21-23] BICs generally require precise geometric conditions and spatially infinite structures, and geometric distortion from the ideal BIC condition causes the formation of *quasi*-BICs, which can exhibit the desirable characteristics of both high Q factors and the ability to couple to far-field radiation because of imperfect destructive interference in the far field.[24,25] To-date, nonlinear responses employing *quasi*-BICs have primarily used metasurfaces[26-28] and metasurfaces combined with nonlinear materials.[29] In addition, a BIC-inspired resonance between a sub-wavelength semiconductor nanorod and optically-engineered substrate was observed to enhance non-linear generation under azimuthally polarized illumination at a single particle level.[20,30]

BICs and *quasi*-BICs were also recently observed in a laterally-confined, one-dimensional (1D) Si nanowire (NW) geometric superlattices (GSLs).[31] A Si NW GSL can be created by periodically modulating the diameter of a Si NW along its axis (Figure 1A). Here, we report the dramatic enhancement of the nonlinear response from a Si NW GSL arising from the intense electromagnetic field enhancement of *quasi*-BICs. The *quasi*-BICs were achieved by purposely detuning the pitch (*p*) of Si NW GSLs from the BIC geometric condition calculated using the finite-element method (FEM). The spectral position of *quasi*-BICs were confirmed by the observation of Fano resonances in the measured linear extinction spectra from single NWs, and enhanced frequency conversion for both second harmonic generation (SHG) and third harmonic generation (THG) was observed when the fundamental frequency was tuned to the *quasi*-BIC spectral position. FEM numerical simulations were performed to understand the origin of localized electromagnetic fields that drive nonlinear processes.

RESULTS AND DISCUSSION

Design and fabrication of Si NW GSLs. Si NW GSLs (Figure 1A) were fabricated by a bottom-up vapor-liquid-solid (VLS) growth process utilizing *in situ* dopant modulation followed by wet-chemical etching (see Methods for details).[32] As shown by an example in Figure 1B, the dopant precursor (diborane, B_2H_6) flow rate was rapidly modulated during VLS growth to encode specific doping levels along the NW axis. Wet-chemical etching with aqueous potassium hydroxide (KOH) solution yielded a well-defined geometric profile reflecting the encoded dopant profile, as shown by a scanning electron microscopy (SEM) image (Figure 1C) and corresponding diameter profile (Figure 1B). The diameter (*d*), etched diameter (*e*), pitch (*p*), and number of unit cells (*N*) of a Si NW GSL were determined by the size of Au catalyst, wet-chemical etching time, and the frequency and time scale of B_2H_6 flow modulation. Au catalysts yielding $d \approx 400$ nm were chosen to achieve optical BIC and *quasi*-BICs at near infrared telecommunication wavelengths where absorptive loss of Si can be reasonably neglected.[31] Based on the SEM image and profile of the fabricated Si NW GSL, in all cases below we consider in the numerical simulations NW GSLs with d = 390 nm, e = 250 nm, and axial lengths of etched and unetched segments each equal to $p/2$.

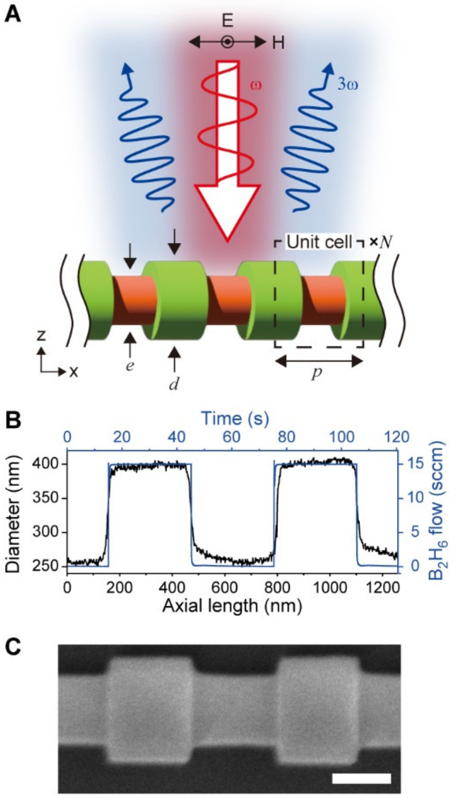

Figure 1. Geometric design. (A) Schematic illustration of the design and geometric parameters of a Si NW GSL illuminated with a TE-polarized plane wave. (B) Recorded B_2H_6 dopant precursor flow profile as a function of time (blue) and diameter profile as a function of axial length (black), yielding d = 390 ± 10, e = 250 ± 10, and p = 631 ± 3 nm. (**C**) SEM image of fabricated Si NW GSL; scale bar, 200 nm.

Local field enhancement at *quasi*-BICs. Under normal incident transverse-electric (TE) polarized plane wave illumination with the electric field (E) perpendicular to the NW axis, a Si NW GSL supports a series of resonances with different azimuthal order m, some of which become BIC and *quasi*-BIC resonances.[31,33] The magnetic field (H) components along the NW axial direction (H_x) of the $m = 0$ and 1 *quasi*-BICs show mode profiles (Figure 2A,B) similar to their corresponding BICs (Figure S1A,B) but with asymmetry introduced from biased plane-wave illumination coming from the z direction.[34] Such *quasi*-BICs from a $p = 600$ nm GSL are manifested in the scattering efficiency (Q_{sca}) spectrum (red curve in Figure 2E) as asymmetric peaks with a Fano lineshape on top of a broader Mie resonance scattering envelope.[31,35] The Fano features at 1029 and 1235 nm are associated with $m = 0$ and 1 *quasi*-BICs of the Si NW GSL, respectively. When p is shortened to $p = 460$ nm, the resonance that was associated with the $m = 1$ *quasi*-BIC blueshifts to the wavelength of 1096 nm and disappears from the spectrum (black curve in Figure 2E) because the $m = 1$ mode decouples from both the external plane wave and the Mie resonance of the same angular channel, indicating the existence of an $m = 1$ optical BIC. In addition, the calculated Q factor (Figure S1C) of the $m = 1$ mode progressively increases and diverges near $p = 460$ nm as the BIC condition is achieved. The wavelength shift and disappearance of Fano features in the Q_{sca} spectrum (Figure S1D) and divergence of Q factor (Figure S1C) are also observed with $m = 0$ mode but at a different p of 419 nm. Disappearance and reappearance of the Fano features as a function of p is more clearly observed in the heat map of Q_{sca} in Figure 2F. As p decreases, the Fano features associated with $m = 0$ and $m = 1$ *quasi*-BICs blueshift and disappear near $p = 460$ and 419 nm, respectively (indicated with white arrows in Figure 2F).

To examine the local field enhancement at BIC and *quasi*-BIC, electric energy enhancement inside the Si NW GSL ($U/U_0 = \iiint \frac{1}{2}\varepsilon|\boldsymbol{E}|^2\,dV / \iiint \frac{1}{2}\varepsilon_0|\boldsymbol{E}_0|^2\,dV$, where ε is the permittivity of the Si and ε_0 is the vacuum permittivity) was calculated. The U/U_0 spectrum of a Si NW GSL with p = 600 nm (red curve in Figure 2G) shows two peaks at 1029 and 1235 nm, which corresponds to the two Fano features in the Q_{sca} spectrum. Note that sharp peak at 889 nm is associated with a higher-order guided resonance[31,36,37], which does not show evidence for formation of an optical BIC (Figure S2A), and broad peak at 897 nm is associated with m = 2 Mie resonance[31] (Figure S2B). In contrast, no U/U_0 enhancement was observed at the wavelength of 1096 nm with p = 460 nm (black curve in Figure 2G) because it is fully decoupled from the radiation continuum. Similarly, the sharp peak at the wavelength of 942 nm, which is associated with m = 0 *quasi*-BIC, also disappears in the U/U_0 spectrum with p = 419 nm, where Si NW GSL satisfies m = 0 BIC condition (Figure S1D). The higher-order guided resonance and m = 2 Mie resonance have also blue shifted outside the wavelength range shown. These results are also exemplified by the U/U_0 heat map in Figure 2H. For both m = 0 and 1 *quasi*-BICs, the U/U_0 is at minimum when p satisfies the BIC condition (indicated with white arrows in Figure 2H). In particular, we show the normalized |**E**| distribution at wavelengths corresponding to the BIC and *quasi*-BIC (Figure 2C,D and Figure S1D). The |**E**| distribution at the *quasi*-BIC condition shows tight confinement and enhancement of local fields in the Si NW GSL compared with that from the Si NW GSL at the BIC condition. Although BICs show much higher Q factor than *quasi*-BICs, the electric field distribution under external incident light clearly illustrates the higher light energy confinement of *quasi*-BICs, making them strong candidates for nonlinear optical effects.

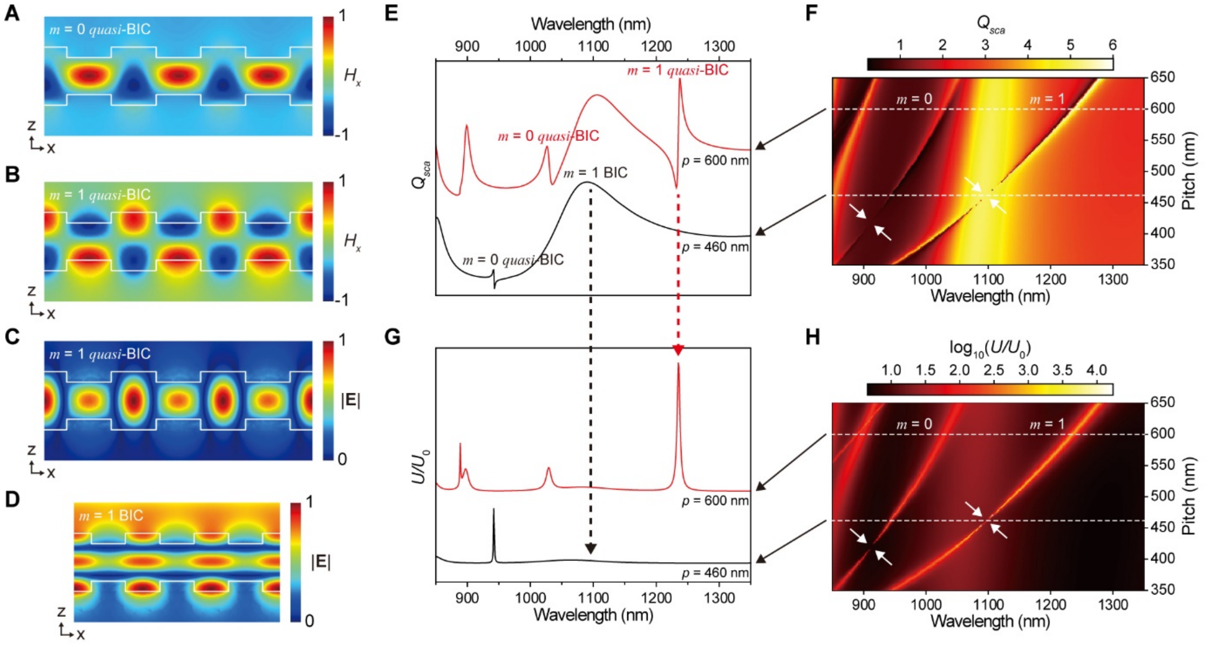

Figure 2. Simulations of near-infrared *quasi*-BICs in a Si NW GSL (d = 390 nm; e = 250 nm; $N = \infty$) illuminated with a TE-polarized plane wave. (**A**) Calculated H_x field distribution of $m = 0$ *quasi*-BIC with p = 600 nm at 1029 nm. (**B**,**C**) Calculated H_x field (panel B) and |**E**| field (panel C) distribution of an $m = 1$ *quasi*-BIC with p = 600 nm at 1235 nm. (**D**) Calculated |**E**| field distribution of a Si NW GSL with p = 460 nm at 1096 nm (the position of the BIC resonance). (**E**) Calculated Q_{sca} of a Si NW GSL with p = 600 nm (red curve) and p = 460 nm (black curve). (**F**) Heat maps of calculated Q_{sca} with various p. (**G**) Calculated U/U_0 of Si NW GSL with p = 600 nm (red curve) and p = 460 nm (black curve). (**H**) Heat maps of calculated $\log_{10}(U/U_0)$ with various p.

Measurement of THG from *quasi*-BICs. To experimentally examine nonlinear optical enhancements from a Si NW GSL, we collected and analyzed both extinction and nonlinear spectra from the same set of GSLs, allowing direct correlations between them. First, extinction spectra were measured to identify the spectral position of *quasi*-BICs within GSLs with N = 40, where different values of p were encoded within segments of individual NWs by terminating both ends of each segment with a uniform diameter section, as illustrated in Figure 3A. An exemplary TE-polarized extinction spectrum is shown in Figure 3B for a NW GSL with $p = 650$ nm, showing two distinct Fano features in the near-infrared region. Second, we measured SHG and THG spectra from the same Si NW GSL sections using a wavelength-tunable femtosecond Ti:sapphire laser with a repetition rate of 80 MHz coupled to an Optical Parametric Oscillator. Figure 3B also displays an exemplary THG intensity spectrum, which exhibits two distinct peaks that match well with the spectral positions of the Fano features in the extinction spectrum of the same NW segment.

To interpret the enhanced nonlinear effects in Si NW GSLs, we calculated both linear and nonlinear optical responses of a finite-size Si NW GSL. In order to account for the beam polarization and spot size used in experiments, simulations utilized TE-polarized Gaussian beams for incident light. The wavelength-dependent beam spot sizes were ~2.8-3.6 μm and ~11-15 μm for the nonlinear experiments with the femtosecond radiation and the extinction measurements, respectively (see Methods). The simulated Q_{sca} spectrum (black circles in Figure 3C), which accounts for the expected beam spot size for extinction measurements at each wavelength, shows a broad Mie resonance scattering envelope and two distinct Fano features, in good agreement with the experimental results. We also note that additional small peak at the wavelength of 1145 nm originates from the finite N value and Gaussian beam excitation.[31,37] Plots of the spatial $|\mathbf{E}_\omega|$ field profiles (Figure 3D,F), which account for the expected beam spot size for nonlinear measurements, show significant local field enhancement consistent with the presence of *quasi*-BICs at the wavelength of each Fano feature. Simulations of the THG spectra (blue curve in Figure 3C) using the third-order non-linear susceptibility of Si reproduce the two primary THG peaks observed in the experimental measurement. Plots of the spatial $|\mathbf{E}_{3\omega}|$ field profiles at the wavelength of each THG peak (Figure 3E,G) show intensity envelopes at the third harmonic frequency (3ω) that correspond to the intensity profile at the fundamental frequency (ω). Thus, the results show that the local field enhancement caused by the *quasi*-BICs at frequency ω drives the nonlinear response at 3ω.

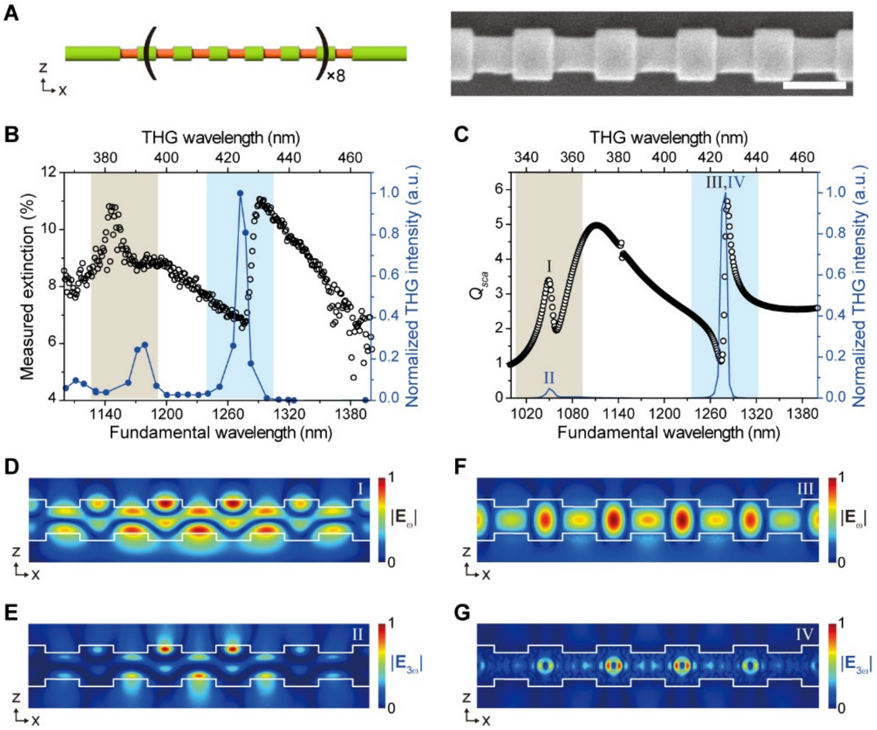

Figure 3. Third harmonic generation from Si NW GSL *quasi*-BICs. (**A**) Schematic (left) and SEM (right) image of a Si NW GSL; scale bar, 500 nm. Geometric parameters are $d = 400 \pm 10$, $e = 250 \pm 10$, and $p = 650 \pm 4$ nm. (**B**,**C**) Measured extinction (black circles) and THG intensity (blue curve) spectra (panel B) and simulated Q_{sca} (black circles) and THG intensity (blue curve) spectra (panel C) of Si NW GSL ($N = 40$) with $p = 650$ nm. Both measured and simulated THG intensity are shown normalized to the maximum. Beige and blue colored areas indicate the

spectral positions corresponding to the $m = 0$ and $m = 1$ *quasi*-BICs, respectively. (**D**,**E**) Calculated |**E**| field distributions near the $m = 0$ *quasi*-BIC (1052 nm) for both fundamental (panel D) and third harmonic (panel E) frequencies in a Si NW GSLs. (**F**,**G**) Calculated |**E**| field distributions near the $m = 1$ *quasi*-BIC (1277 nm) for both fundamental (panel F) and third harmonic (panel G) frequencies in a Si NW GSL. Only 5 unit cells from the center of Si NW GSLs are shown for brevity.

Measurement of SHG from *quasi*-BICs. Figure 4A displays extinction and SHG spectra for the same Si NW GSL shown in Figure 3. Similar to THG, peaks in the SHG spectrum are observed at 2ω frequencies correlated with the ω fundamental frequencies of the *quasi*-BICs. Because bulk Si is centrosymmetric, SHG is expected to arise from the breaking of symmetry at the NW surface and from field gradients due to resonant modes or tightly focused beams.[1,3,38-43] As shown in Figure 4B and 4D, the field enhancements at the NW surface are apparent from top view and cross-sectional $|\mathbf{E}_\omega|$ field profiles of the $m = 0$ and $m = 1$ *quasi*-BICs, respectively, and enhancement of SHG signals would thus be expected to occur as a result of enhanced fields close to the NW surface. Although enhancement of SHG from centrosymmetric nanostructures is often expected to occur as a result of enhanced fields components normal ($E_\perp$) to the surface, contributions from tangential fields ($E_\parallel$) at the surface as well as from strong field gradients ($[\mathbf{E}\cdot\nabla]\mathbf{E}$) in the Si NW have to be considered when under optical resonance conditions.[43] In particular, Figure 4C and 4E display $|[\mathbf{E}_\omega\cdot\nabla]\mathbf{E}_\omega|$ spatial distributions for the $m = 0$ and $m = 1$ *quasi*-BICs, respectively, and the plots show strong field gradients inside the Si NW GSL. Figure 4F displays a spectra of the surface-integrated $|E_\perp|^2$ and $|E_\parallel|^2$ quantities and the volume-integrated $|[\mathbf{E}_\omega\cdot\nabla]\mathbf{E}_\omega|^2$ quantity inside the Si NW GSL. The spectra show reasonable qualitative agreement with the SHG signal measured from the Si NW GSL, confirming that all three SHG mechanisms are likely contributors to the SHG signals. However, we also found the SHG signals to vary substantially between different Si NW GSLs and the trends to be less predictable compared to the THG signals (Figure S3A,B). We attribute this variability to the sensitivity of the SHG signal to the NW surface and the potential for different mechanisms to dominate depending on the structure; thus, we primarily focus on the THG signal, which reflects electric field enhancement from *quasi*-BICs throughout the bulk of the NW due to the non-zero third-order susceptibility of Si. We note that the experimental SHG peak attributed to the $m = 0$ *quasi*-BIC is shifted with respect to the Fano feature in the extinction spectrum and shifted relative to the THG peak, while in simulations no shift is observed. We attribute these differences to the effects of the focused beam used in experiments, the strong wavelength dependence of non-linear susceptibilities of Si at near infrared telecommunication wavelengths,[16] and to ambiguities in the exact values of susceptibilities to use in simulations due to variability in the experimental data reported.[44]

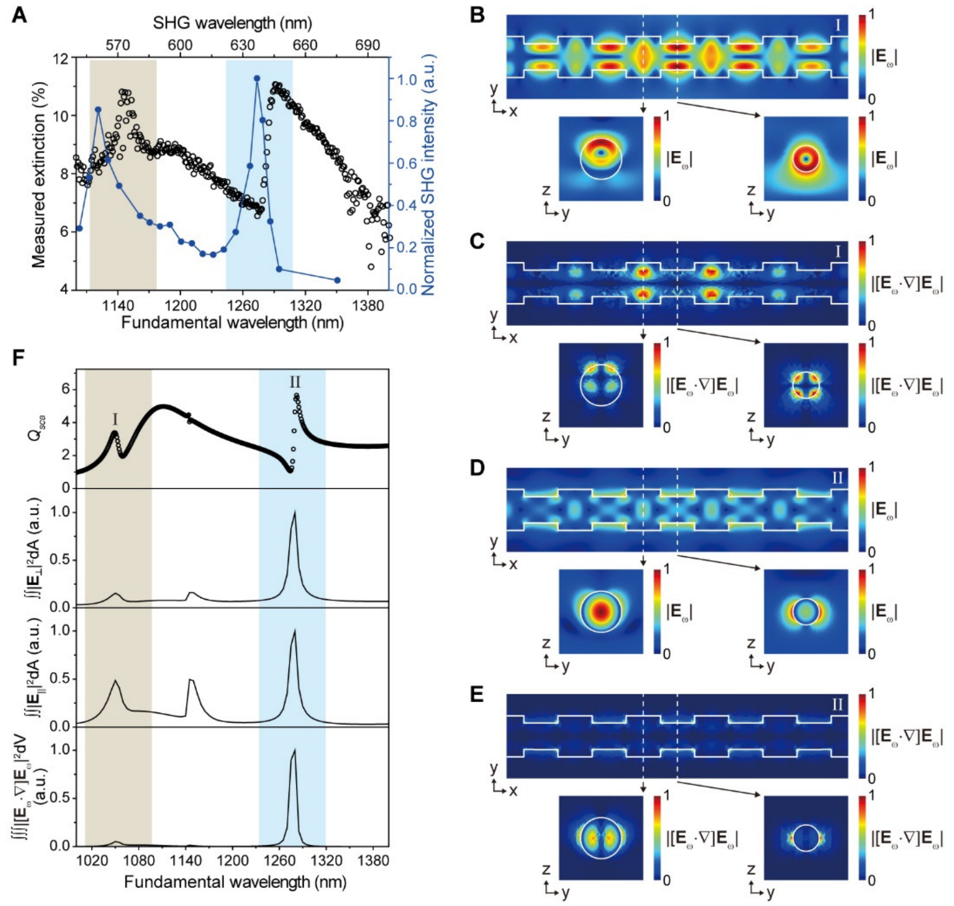

Figure 4. Second harmonic generation from Si NW GSL *quasi*-BICs. (**A**) Measured extinction (black circles) and SHG intensity (blue curve) spectra of a Si NW GSL with $d = 400 \pm 10$, $e = 250 \pm 10$, and $p = 650 \pm 4$ nm with $N = 40$. SHG curves are shown normalized to the maximum. Beige and blue colored areas indicate the spectral positions corresponding to the $m = 0$ and $m = 1$ *quasi*-BICs, respectively. (**B-E**) Calculated $|\mathbf{E}_\omega|$ (panels B,D) and $|[\mathbf{E}_\omega \cdot \nabla]\mathbf{E}_\omega|$ (panels C,E) distributions near the $m = 0$ (panels B,C) and the $m = 1$ (panels D,E) *quasi*-BICs at the fundamental wavelengths of 1052 nm and 1277 nm, respectively. Field distributions for both axial cross sections through the middle of the NW (top) and radial cross-sections (bottom) are shown. White dashed lines denote the axial positions of the radial cross sections. (**F**) Simulated Q_{sca} (top), surface-integrated $|E_\perp|^2$ (upper middle), surface-integrated $|E_\parallel|^2$ (lower middle), and

volume-integrated $|[\mathbf{E}_\omega \cdot \nabla]\mathbf{E}_\omega|^2$ inside the Si NW GSL (bottom). Beige and blue colored areas indicate the spectral positions corresponding to the *m* = 0 and *m* = 1 *quasi*-BICs, respectively. Simulated $\iint |E_\perp|^2 \, dA$, $\iint |E_\parallel|^2 \, dA$ and $\iiint |[\mathbf{E}_\omega \cdot \nabla]\mathbf{E}_\omega|^2 \, \mathrm{dV}$ are shown normalized to the maximum.

Geometrically-tunable THG. We explored the ability to tune the THG spectral efficiency by geometric design of the NW GSL, which is possible because of the strong dependence of U/U_0 and Q factor on *p*. As shown schematically in Figure 5A, distinct GSLs with different *p* values (520, 600, and 650 nm) were synthesized within a single NW to minimize variation in *d* and *e*, and spectra were separately measured from each *N* = 40 GSL. The measured extinction spectra (Figure 5B) show Fano features associated with *quasi*-BICs, with the resonant wavelength, linewidth, and amplitude strongly dependent on *p*. The results are in reasonable agreement with simulated spectra (Figure 5C) based on the measured geometric parameters. Note that a Si NW GSL with *p* near 460 nm satisfies the *m* = 1 BIC condition with high Q factor (*c.f.* Figure 2 and Figure S1C), so the measured GSLs reflect three *quasi*-BIC frequencies that are progressively detuned to lower frequencies from the anticipated BIC frequency.

The experimental THG spectra (Figure 5D) show several peaks at 3ω frequencies that correspond to fundamental ω frequencies identified for the *quasi*-BICs from experimental extinction spectra. Interestingly, the maximum THG enhancement was observed with the intermediate *quasi*-BIC resonance using *p* = 600 nm, even though the resonance closer to the BIC (with *p* = 520 nm) might have initially been expected to maximize the enhancement. For simulations of THG spectra (Figure 5E) to reproduce the *p*-dependent nonlinear enhancement, we found they had to realistically account for the focused femtosecond laser beam, which causes a distribution of angles (θ) and corresponding wavevectors (*k*) to be incident on the GSL (Figure S4). An increase in θ and *k* from zero results in a decrease of both the Q factor and U/U_0 of *quasi*-BICs, as shown in Figure 5F and 5G, respectively. However, the decrease is the most rapid for *quasi*-BIC resonances closer to the BIC condition. Thus, detuning of *quasi*-BIC resonances from the BIC has the disadvantage of decreasing the Q factor and U/U_0 for $k = 0$, but it also has the advantage of decreasing the sensitivity of the resonance to deviations from the ideal $k = 0$ condition. For instance, in the case of $p = 600$ nm, U/U_0 at $k = 0$ is smaller than that of $p = 520$ nm, but U/U_0 at $k \neq 0$ is much larger (Figure 5G). Consequently, as shown in Figure 5H, the weighted-integration of U/U_0 at $p = 600$ nm over the experimental θ distribution shows a larger value than that of $p = 520$ and 650 nm, explaining why maximal THG was observed with p = 600 nm. This *quasi*-BIC resonance thus represents a balance between the capacity to trap light and couple to the external radiation continuum under experimentally realistic illumination conditions. We further note that tuning the geometric parameter *e* in addition to *p* would provide yet another opportunity to tune the geometry to maximize harmonic generation (Figure S5).

In terms of THG signal enhancement, the Si NW GSL with $p = 600$ nm shows ~28.3 times larger THG enhancement (Figure S3C) compared to a comparable cylindrical Si NW ($d = 410 \pm 3$ nm). Indeed, all the Si NW GSLs show higher THG enhancement at the *quasi-BIC* wavelengths relative to that of cylindrical NW (Figure 5D), in which local field enhancement is solely attributed to Mie resonances (Figure S3D). Furthermore, we measured the peak THG power ($P_p(3\omega)$) of Si NW GSL with $p = 600$ nm with respect to the excitation peak power ($P_p(\omega)$), as shown in the inset of Figure 5D ($\lambda_{pump} = 1240$ nm). With increasing pump power, the THG power increases following the cubic law with a fit yielding an exponent of 2.92 ± 0.19. The estimated normalized THG conversion efficiency defined by $\zeta = P_p(3\omega)/[P_p(\omega)]^3$ was 9.7×10^{-12}

W^{-2} at the peak pump power of $P_P(\omega) = 83.85$ W (peak intensity of ~3.3 GW/cm^2), which is within the range of the previous reports on THG conversion efficiency in Si nanostructures.[15,19,26,28] However, a Si NW GSLs provides much smaller footprint compared to metasurfaces, making it a promising candidate for nanophotonic applications. For example, if we used only the power incident on the NW projected area to calculate the efficiency, the value would become 2.4×10^{-9} W^{-2}. In addition, the simulated THG conversion efficiency for Si NW GSLs depends on N, first increasing with increasing N but then plateauing at $N \sim 40$ under an excitation beam spot size of ~3.2 μm (Figure S6). This indicates that Si NW GSLs with projected area footprints smaller than ~10 μm^2 can support *quasi*-BICs for efficient harmonic generation while retaining more than 90% of the efficiency of a larger structure.

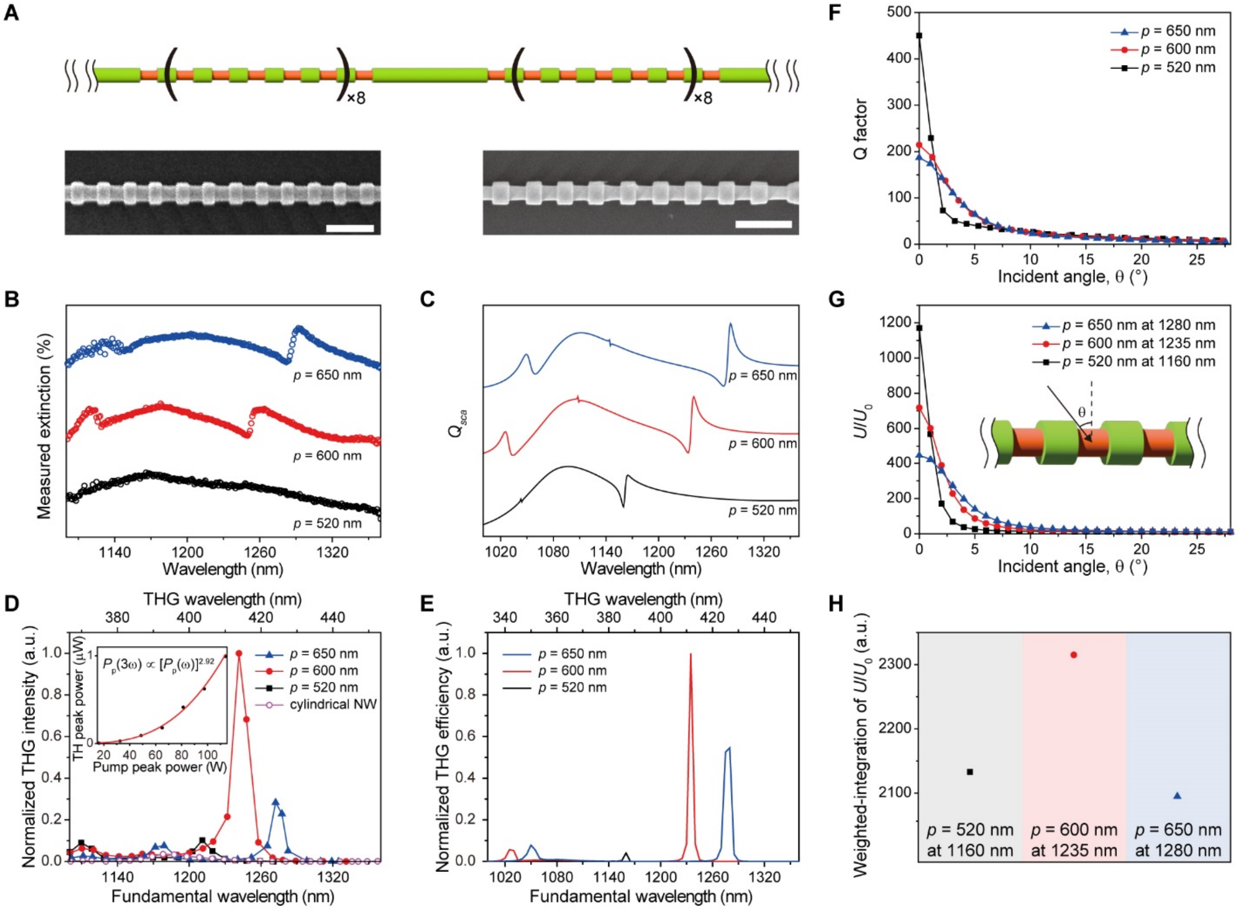

Figure 5. Third harmonic generation with geometrically-tuned *quasi*-BICs. (**A**) Schematic (top) and SEM images (bottom) of a Si NW GSL; all scale bars, 1 μm. Geometric parameters are $d = 400 \pm 10$, $e = 260 \pm 10$, and $p = 520 \pm 5$ nm (bottom left panel) and $d = 390 \pm 5$, $e = 250 \pm 10$, and $p = 600 \pm 10$ nm (bottom right panel). (**B,C**) Measured extinction (panel B) and simulated Q_{sca} (panel C) spectra of Si NW GSLs ($N = 40$) with $p = 520$ (black), 600 (red), and 650 nm (blue). (**D**) Measured THG intensities spectra of a cylindrical NW (violet open circles) and Si NW GSLs with $p = 520$ (black closed squares), 600 (red closed circles), and 650 nm (blue closed triangles). THG intensities are normalized to the maximum intensity measured with $p = 600$ nm. Inset: THG peak power (black circles) as a function of fundamental incident peak power from the Si NW GSL with $p = 600$ nm with excitation at 1240 nm. Red line represents a fit to the

data. (**E**) Calculated THG efficiencies of Si NW GSLs ($N = 40$) with $p = 520$ (black), 600 (red), and 650 nm (blue). THG intensities are normalized to the maximum intensity measured with $p =$ 600 nm. (**F**) Calculated Q factor as a function of incident angle (θ) corresponding to wavevectors (k) in Si NW GSLs ($d = 390$ nm; $e = 250$ nm; $N = \infty$) with $p = 520$ (black closed squares), 600 (red closed circles), and 650 nm (blue closed triangles). The incident angle (θ) was calculated with $(2\pi/p)k = (\omega/c)\sin\theta$, where c is speed of light. Q factor was obtained with absorptive loss of Si. (**G**) Calculated U/U_0 of Si NW GSLs ($d = 390$ nm; $e = 250$ nm; $N = \infty$) with $p = 520$ (black closed squares), 600 (red closed circles), and 650 nm (blue closed triangles) under TE-polarized plane wave as a function of various incident angle (θ). The U/U_0 was obtained at the wavelength at which a maximum THG enhancement was generated. (**H**) Weighted-integration of U/U_0 for Si NW GSLs ($d = 390$ nm; $e = 250$ nm; $N = \infty$) with p = 520 (black closed square), 600 (red closed circle), and 650 nm (blue closed triangle) at the wavelengths of 1160, 1235, and 1280 nm, respectively. For each incident angle, weighted U/U_0 were calculated considering a Gaussian distribution in the k-space with waist radius determined by the wavelength and effective numerical aperture of the objective lens used in experiments.

SUMMARY AND CONCLUSIONS

We have observed dramatic enhancement of nonlinear response in single Si NW GSLs as a result of *quasi*-BIC resonances, with the spectral position and magnitude of enhancement controlled by geometric tuning of the GSL structure. Compared to a cylindrical Si NW of similar diameter, the Si NW GSL demonstrated more than an order of magnitude larger THG signal. Although this report focuses on enhancement of SHG and THG from optical BICs within single silicon nanostructures, our approach also has the potential to enhance higher-order parametric nonlinear effects such as four wave mixing and fifth harmonic generation at the nanoscale.[30] Moreover, the Si NW GSLs demonstrated herein offer a versatile platform for the design of more complex structures and active electronic devices using the bottom-up growth process. For example, *p–i–n* superlattices can be encoded within a Si NW GSL,[45,46] enabling photodetection and static electric field effects[47-49] to be explored on conjunction with *quasi*-BIC resonances. We believe that this study represents a meaningful step toward the development of nonlinear subwavelength light sources.

MATERIALS AND METHODS

Fabrication of Si NW GSLs. Si NWs were grown in a home-built chemical vapor deposition system. Au catalysts of diameters 400 nm (Sigma-Aldrich) were immobilized on Si/SiO_2 substrates with polylysine (Sigma-Aldrich) and cleaned in a UV ozone cleaner (Samco UV-1). The substrate was then inserted into a 1 inch hot-wall tube furnace (Lindberg Blue M) and heated to the growth temperature. Silane (SiH_4, Voltaix) and diborane (B_2H_6, 1000 ppm in H_2, Voltaix) served as the precursors for the NWs. HCl (Matheson TriGas, 5 N) was used for surface chlorination, and H_2 (Matheson TriGas, 5N semiconductor grade) was used as the carrier gas. All NWs were nucleated and grown at 530 °C and a total pressure of 40 Torr, with 2 sccm of SiH_4 and 4 sccm of HCl. The p-type sections of Si NWs were grown using a B_2H_6 gas flow of 15 sccm. The flow of H_2 carrier gas was varied between 179 and 194 sccm, depending on the dopant gas flow, to maintain a constant SiH_4 partial pressure. To encode GSL profiles, doping modulation was performed during Si NW growth by controlling the B_2H_6 flow. The resulting growth substrate was dipped into diluted BHF (50 volume %) for 5 s to remove native oxide and subsequently immersed in aqueous KOH solution (20 weight %) at room temperature for times varying between 3 min to 5 min, depending on the intended etch depth. The growth substrate was quenched in acetic acid (2 volume %) and rinsed in water and isopropanol. Next, NW GSLs were wet-transferred from the substrates on which they were grown onto glass microscopy slides (Fisher Scientific) coated with ~3 nm of ITO by sputtering (Kurt Lesker PVD 75) to facilitate scanning electron microscopy (SEM) imaging. The glass microscopy slides were briefly rinsed with isopropanol and blown dry with N_2. SEM imaging was performed with an FEI Helios 600 Nanolab Dual Beam System.

Extinction measurements. A supercontinuum laser (NKT Photonics; SuperK Extreme EXB-6) coupled to a monochromator (Princeton Instruments; Acton SP2300) was used as the light source. The laser was linearly polarized by an uncoated Glan-Thompson calcite polarizer (10GT04, Newport) and split evenly into a reference and probe beam for balanced detection with a Nirvana balanced photoreceiver (Newport; Nirvana Auto-Balanced Photoreceiver 2017). The probe beam was directed to a pair of matched reflective objectives (Thorlabs; LMM-40X-P01; numerical aperture 0.5). To achieve *quasi*-plane wave illumination, the probe beam deeply under-filled the back aperture of the objective. The optical power was collected with the probe beam placed on and off the NW by modulating the substrate position using a piezo positioner (Mad City Labs; Nano-LP 200). Measured extinction (%) was calculated as $(1 - T) \times 100$ with $T = I/I_0$, where I and I_0 are transmitted powers collected with the beam on and off the NW, respectively.

Nonlinear measurements. A Chameleon Ultra II Ti:sapphire femtosecond laser with a repetition rate of 80 MHz coupled to an Optical Parametric Oscillator (OPO) was used as the excitation source. A 100× objective (NA = 0.95) was used to focus the TE-polarized excitation beam and collect the THG and SHG signals. Nonlinear spectroscopy was performed by continuously tuning the OPO output from 1100 nm to 1400 nm and recording the SHG and THG spectra for every excitation wavelength. The raw signals were fit to a Gaussian peak and integrated. THG spectra were normalized by the cubic of the excitation power and SHG spectra were normalized by the square of the excitation power.

Numerical simulations. We used the finite element method (FEM) (COMSOL Multiphysics) to calculate linear and nonlinear optical responses. The structural parameters used in the simulations were determined based on the SEM images of the fabricated Si NW GSLs (Figure 1B,C). For infinite-size Si NW GSL, one period of a Si NW GSL was split in half along NW axial direction by a perfect electric conductor plane and placed between periodic boundaries in the axial direction. The air region surrounding Si NW GSL was terminated by a perfectly matched layer and scattering boundary. Q_{sca} was calculated by integrating Poynting vectors across the outer surface of a Si NW GSL and dividing by the incident power considering the projected area of the NW GSL. The THG response was calculated using coupled electromagnetic models. First, linear scattering was simulated at the pump wavelength and nonlinear polarization induced inside the Si NW GSL was obtained. Then, nonlinear polarization was employed as a source for the electromagnetic simulation at the THG wavelength to obtain the generated THG field. THG power was calculated by integrating Poynting vectors across the outer surface of a Si NW GSL at the THG wavelength. THG powers were normalized by the cubic of the excitation power considering the projected area of the NW GSL. The nonlinear susceptibility function $\chi^{(3)}$ was considered as a tensor corresponding to the cubic crystallographic point group with $\chi^{(3)}_{xxxx} = 2.45 \times 10^{-19}$ m^2/V^2 at wavelength 1550 nm.[26,44,50] The refractive indices and extinction coefficients of Si were taken from the literature.[51]

ASSOCIATED CONTENT

Supporting Information

Figures S1, which shows additional simulation results of optical BICs in a Si NW GSL, Figure S2, which shows H_x field distributions of a higher-order guided resonance and $m = 2$ Mie resonance, Figure S3, which shows measured extinction, SHG, and THG spectra of Si NW GSLs ($p = 520$ and 600 nm) and a cylindrical Si NW ($d = 410$ nm), Figure S4, which shows the effect of beam spot size on the distribution of k-vectors incident on a NW GSL, Figure S5, which shows the effect of the geometric parameter e on harmonic generation from a NW GSL, and Figure S6, which shows simulated THG conversion efficiencies from Si NW GSLs with various N.

AUTHOR INFORMATION

Corresponding Author

*Email: hayk.harutyunyan@emory.edu, jfcahoon@unc.edu

Author contributions

J.F.C. and H.H. conceived the research and supervised the project. J.-S.P., C.L., Y.T., C.G.E.M., T.S.T., and S.K. performed the experiments. J.-S.P., C.L., K.-H.K., H.H., and J.F.C, performed the theoretical analyses. J.-S.P. and J.F.C. wrote the manuscript based on the input from all the authors. All authors contributed to writing and editing the manuscript.

Notes

The authors declare no competing financial interests.

ACKNOWLEDGMENT

This research was primarily supported by the National Science Foundation (NSF) through grant DMR-2121643. This work made use of instrumentation at the Chapel Hill Analytical and Nanofabrication Laboratory (CHANL), a member of the North Carolina Research Triangle

Nanotechnology Network (RTNN), which is supported by the National Science Foundation, Grant ECCS-2025064, as part of the National Nanotechnology Coordinated Infrastructure, NNCI. H.H. acknowledges support from the Department of Energy (DE-SC0020101). Optical measurements by Y.T. were supported by the NSF through Grant CBET-2231857. K.-H.K. acknowledges support from an IITP grant funded by the Korean government (MSIT) (no. 2022-0-00897).

REFERENCES

1. Boyd, R. W. In *Nonlinear Optics*, 3rd ed.; Elsevier: New York, 2008.
2. Aouani, H.; Rahmani, M.; Navarro-Cía, M.; Maier, S. A. Third-harmonic-upconversion enhancement from a single semiconductor nanoparticle coupled to a plasmonic antenna. *Nat. Nanotechnol.* **2014**, *9* (4), 290-294.
3. Smirnova, D.; Kivshar, Y. S. Multipolar nonlinear nanophotonics. *Optica* **2016**, *3* (11), 1241-1255.
4. Bonacina, L.; Brevet, P.-F.; Finazzi, M.; Celebrano, M. Harmonic generation at the nanoscale. *J. Appl. Phys.* **2020**, *127* (23), 230901.
5. Liu, T.; Xiao, S.; Li, B.; Gu, M.; Luan, H.; Fang, X. Third- and Second-Harmonic Generation in All-Dielectric Nanostructures: A Mini Review. *Front. Nanotechnol.* **2022**, *4*, 891892, Mini Review.
6. Hanke, T.; Krauss, G.; Träutlein, D.; Wild, B.; Bratschitsch, R.; Leitenstorfer, A. Efficient Nonlinear Light Emission of Single Gold Optical Antennas Driven by Few-Cycle Near-Infrared Pulses. *Phys. Rev. Lett.* **2009**, *103* (25), 257404.
7. Harutyunyan, H.; Volpe, G.; Quidant, R.; Novotny, L. Enhancing the Nonlinear Optical Response Using Multifrequency Gold-Nanowire Antennas. *Phys. Rev. Lett.* **2012**, *108* (21), 217403.
8. Kauranen, M.; Zayats, A. V. Nonlinear plasmonics. *Nat. Photonics* **2012**, *6* (11), 737-748.
9. Metzger, B.; Hentschel, M.; Schumacher, T.; Lippitz, M.; Ye, X.; Murray, C. B.; Knabe, B.; Buse, K.; Giessen, H. Doubling the Efficiency of Third Harmonic Generation by Positioning ITO Nanocrystals into the Hot-Spot of Plasmonic Gap-Antennas. *Nano Lett.* **2014**, *14* (5), 2867-2872.
10. Han, S.; Kim, H.; Kim, Y. W.; Kim, Y.-J.; Kim, S.; Park, I.-Y.; Kim, S.-W. High-harmonic generation by field enhanced femtosecond pulses in metal-sapphire nanostructure. *Nat. Commun.* **2016**, *7* (1), 13105.
11. Novikov, S. M.; Frydendahl, C.; Beermann, J.; Zenin, V. A.; Stenger, N.; Coello, V.; Mortensen, N. A.; Bozhevolnyi, S. I. White Light Generation and Anisotropic Damage in Gold Films near Percolation Threshold. *ACS Photonics* **2017**, *4* (5), 1207-1215.
12. Rahimi, E.; Gordon, R. Nonlinear plasmonic metasurfaces. *Adv. Opt. Mater.* **2018**, *6* (18), 1800274.

13. Shcherbakov, M. R.; Neshev, D. N.; Hopkins, B.; Shorokhov, A. S.; Staude, I.; Melik-Gaykazyan, E. V.; Decker, M.; Ezhov, A. A.; Miroshnichenko, A. E.; Brener, I.; et al. Enhanced Third-Harmonic Generation in Silicon Nanoparticles Driven by Magnetic Response. *Nano Lett.* **2014**, *14* (11), 6488-6492.
14. Shcherbakov, M. R.; Shorokhov, A. S.; Neshev, D. N.; Hopkins, B.; Staude, I.; Melik-Gaykazyan, E. V.; Ezhov, A. A.; Miroshnichenko, A. E.; Brener, I.; Fedyanin, A. A.; et al. Nonlinear Interference and Tailorable Third-Harmonic Generation from Dielectric Oligomers. *ACS Photonics* **2015**, *2* (5), 578-582.
15. Yang, Y.; Wang, W.; Boulesbaa, A.; Kravchenko, I. I.; Briggs, D. P.; Puretzky, A.; Geohegan, D.; Valentine, J. Nonlinear Fano-Resonant Dielectric Metasurfaces. *Nano Lett.* **2015**, *15* (11), 7388-7393.
16. Shorokhov, A. S.; Melik-Gaykazyan, E. V.; Smirnova, D. A.; Hopkins, B.; Chong, K. E.; Choi, D.-Y.; Shcherbakov, M. R.; Miroshnichenko, A. E.; Neshev, D. N.; Fedyanin, A. A.; et al. Multifold Enhancement of Third-Harmonic Generation in Dielectric Nanoparticles Driven by Magnetic Fano Resonances. *Nano Lett.* **2016**, *16* (8), 4857-4861.
17. Grinblat, G.; Li, Y.; Nielsen, M. P.; Oulton, R. F.; Maier, S. A. Enhanced Third Harmonic Generation in Single Germanium Nanodisks Excited at the Anapole Mode. *Nano Lett.* **2016**, *16* (7), 4635-4640.
18. Wang, L.; Kruk, S.; Xu, L.; Rahmani, M.; Smirnova, D.; Solntsev, A.; Kravchenko, I.; Neshev, D.; Kivshar, Y. Shaping the third-harmonic radiation from silicon nanodimers. *Nanoscale* **2017**, *9* (6), 2201-2206.
19. Chen, S.; Rahmani, M.; Li, K. F.; Miroshnichenko, A.; Zentgraf, T.; Li, G.; Neshev, D.; Zhang, S. Third Harmonic Generation Enhanced by Multipolar Interference in Complementary Silicon Metasurfaces. *ACS Photonics* **2018**, *5* (5), 1671-1675.
20. Koshelev, K.; Kruk, S.; Melik-Gaykazyan, E.; Choi, J.-H.; Bogdanov, A.; Park, H.-G.; Kivshar, Y. Subwavelength dielectric resonators for nonlinear nanophotonics. *Science* **2020**, *367* (6475), 288-292.
21. Hsu, C. W.; Zhen, B.; Lee, J.; Chua, S.-L.; Johnson, S. G.; Joannopoulos, J. D.; Soljačić, M. Observation of trapped light within the radiation continuum. *Nature* **2013**, *499* (7457), 188-191.
22. Hsu, C. W.; Zhen, B.; Stone, A. D.; Joannopoulos, J. D.; Soljačić, M. Bound states in the continuum. *Nat. Rev. Mater.* **2016**, *1* (9), 16048.
23. Koshelev, K.; Favraud, G.; Bogdanov, A.; Kivshar, Y.; Fratalocchi, A. Nonradiating photonics with resonant dielectric nanostructures. *Nanophotonics* **2019**, *8* (5), 725-745.
24. Koshelev, K.; Lepeshov, S.; Liu, M.; Bogdanov, A.; Kivshar, Y. Asymmetric Metasurfaces with High-*Q* Resonances Governed by Bound States in the Continuum. *Phys. Rev. Lett.* **2018**, *121* (19), 193903.
25. Li, S.; Zhou, C.; Liu, T.; Xiao, S. Symmetry-protected bound states in the continuum supported by all-dielectric metasurfaces. *Phys. Rev. A* **2019**, *100* (6), 063803.
26. Koshelev, K.; Tang, Y.; Li, K.; Choi, D.-Y.; Li, G.; Kivshar, Y. Nonlinear Metasurfaces Governed by Bound States in the Continuum. *ACS Photonics* **2019**, *6* (7), 1639-1644.

27. Liu, Z.; Xu, Y.; Lin, Y.; Xiang, J.; Feng, T.; Cao, Q.; Li, J.; Lan, S.; Liu, J. High-*Q* Quasibound States in the Continuum for Nonlinear Metasurfaces. *Phys. Rev. Lett.* **2019**, *123* (25), 253901.
28. Yang, G.; Dev, S. U.; Allen, M. S.; Allen, J. W.; Harutyunyan, H. Optical Bound States in the Continuum Enabled by Magnetic Resonances Coupled to a Mirror. *Nano Lett.* **2022**, *22* (5), 2001-2008.
29. Bernhardt, N.; Koshelev, K.; White, S. J. U.; Meng, K. W. C.; Fröch, J. E.; Kim, S.; Tran, T. T.; Choi, D.-Y.; Kivshar, Y.; Solntsev, A. S. Quasi-BIC Resonant Enhancement of Second-Harmonic Generation in WS_2 Monolayers. *Nano Lett.* **2020**, *20* (7), 5309-5314.
30. Carletti, L.; Kruk, S. S.; Bogdanov, A. A.; De Angelis, C.; Kivshar, Y. High-harmonic generation at the nanoscale boosted by bound states in the continuum. *Phys. Rev. Res.* **2019**, *1* (2), 023016.
31. Kim, S.; Kim, K.-H.; Cahoon, J. F. Optical Bound States in the Continuum with Nanowire Geometric Superlattices. *Phys. Rev. Lett.* **2019**, *122* (18), 187402.
32. Hill, D. J.; Teitsworth, T. S.; Kim, S.; Christesen, J. D.; Cahoon, J. F. Encoding Highly Nonequilibrium Boron Concentrations and Abrupt Morphology in p-Type/n-Type Silicon Nanowire Superlattices. *ACS Appl. Mater. Interfaces* **2017**, *9* (42), 37105-37111.
33. Fan, P.; Yu, Z.; Fan, S.; Brongersma, M. L. Optical Fano resonance of an individual semiconductor nanostructure. *Nat. Mater.* **2014**, *13* (5), 471-475.
34. Abujetas, D. R.; Paniagua-Domínguez, R.; Sánchez-Gil, J. A. Unraveling the Janus Role of Mie Resonances and Leaky/Guided Modes in Semiconductor Nanowire Absorption for Enhanced Light Harvesting. *ACS Photonics* **2015**, *2* (7), 921-929.
35. Melik-Gaykazyan, E.; Koshelev, K.; Choi, J.-H.; Kruk, S. S.; Bogdanov, A.; Park, H.-G.; Kivshar, Y. From Fano to Quasi-BIC Resonances in Individual Dielectric Nanoantennas. *Nano Lett.* **2021**, *21* (4), 1765-1771.
36. Fan, S.; Joannopoulos, J. D. Analysis of guided resonances in photonic crystal slabs. *Phys. Rev. B* **2002**, *65* (23), 235112.
37. Kim, S.; Kim, K.-H.; Hill, D. J.; Park, H.-G.; Cahoon, J. F. Mie-coupled bound guided states in nanowire geometric superlattices. *Nat. Commun.* **2018**, *9* (1), 2781.
38. Guyot-Sionnest, P.; Chen, W.; Shen, Y. R. General considerations on optical second-harmonic generation from surfaces and interfaces. *Phys. Rev. B: Condens. Matter Mater. Phys.* **1986**, *33* (12), 8254-8263.
39. Galli, M.; Gerace, D.; Welna, K.; Krauss, T. F.; O'Faolain, L.; Guizzetti, G.; Andreani, L. C. Low-power continuous-wave generation of visible harmonics in silicon photonic crystal nanocavities. *Opt. Express* **2010**, *18* (25), 26613-26624.
40. Huo, B.; Wang, X.; Chang, S.; Zeng, M.; Zhao, G. Second harmonic generation of individual centrosymmetric sphere excited by a tightly focused beam. *J. Opt. Soc. Am. B* **2011**, *28* (11), 2702-2711.
41. Dev Choudhury, B.; Sahoo, P. K.; Sanatinia, R.; Andler, G.; Anand, S.; Swillo, M. Surface second harmonic generation from silicon pillar arrays with strong geometrical dependence. *Opt. Lett.* **2015**, *40* (9), 2072-2075.
42. Cazzanelli, M.; Schilling, J. Second order optical nonlinearity in silicon by symmetry breaking. *Appl. Phys. Rev.* **2016**, *3* (1), 011104.

43. Wiecha, P. R.; Arbouet, A.; Girard, C.; Baron, T.; Paillard, V. Origin of second-harmonic generation from individual silicon nanowires. *Phys. Rev. B* **2016**, *93* (12), 125421.
44. Hon, N. K.; Soref, R.; Jalali, B. The Third-Order Nonlinear Optical Coefficients of Si, Ge, and $Si_{1-x}Ge_x$ in the Midwave and Longwave Infrared. *J. Appl. Phys.* **2011**, *110*, 011301.
45. Hill, D. J.; Teitsworth, T. S.; Ritchie, E. T.; Atkin, J. M.; Cahoon, J. F. Interplay of Surface Recombination and Diode Geometry for the Performance of Axial p–i–n Nanowire Solar Cells. *ACS Nano* **2018**, *12* (10), 10554-10563.
46. Teitsworth, T. S.; Hill, D. J.; Litvin, S. R.; Ritchie, E. T.; Park, J.-S.; Custer, J. P.; Taggart, A. D.; Bottum, S. R.; Morley, S. E.; Kim, S.; et al. Water splitting with silicon p–i–n superlattices suspended in solution. *Nature* **2023**, *614* (7947), 270-274.
47. Germer, T. A.; Kołasin-acuteski, K. W.; Stephenson, J. C.; Richter, L. J. Depletion-electric-field-induced second-harmonic generation near oxidized GaAs(001) surfaces. *Phys. Rev. B* **1997**, *55* (16), 10694-10706.
48. Ren, M.-L.; Berger, J. S.; Liu, W.; Liu, G.; Agarwal, R. Strong modulation of second-harmonic generation with very large contrast in semiconducting CdS via high-field domain. *Nat. Commun.* **2018**, *9* (1), 186.
49. Zhang, B.; Stehr, J. E.; Chen, P. P.; Wang, X.; Ishikawa, F.; Chen, W. M.; Buyanova, I. A. Anomalously Strong Second-Harmonic Generation in GaAs Nanowires via Crystal-Structure Engineering. *Adv. Funct. Mater.* **2021**, *31* (36), 2104671.
50. Xu, L.; Rahmani, M.; Zangeneh Kamali, K.; Lamprianidis, A.; Ghirardini, L.; Sautter, J.; Camacho-Morales, R.; Chen, H.; Parry, M.; Staude, I.; et al. Boosting third-harmonic generation by a mirror-enhanced anapole resonator. *Light: Sci. & Appl.* **2018**, *7*, 44.
51. Green, M. A. Self-consistent optical parameters of intrinsic silicon at 300K including temperature coefficients. *Sol. Energy Mater. and Sol. Cells* **2008**, *92*, 1305-1310.

For Table of Contents Only

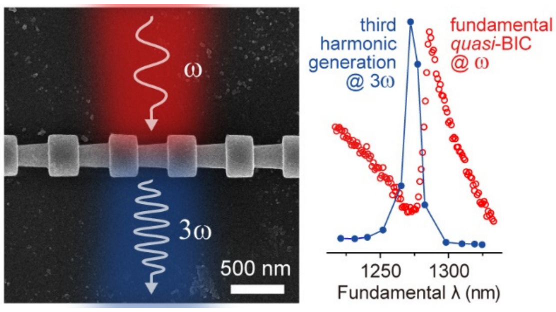

Supporting Information for:

Optical Nonlinearity in Silicon Nanowires Enabled by Bound States in the Continuum

Jin-Sung Park[†]*, Chentao Li*[§]*, Kyoung-Ho Kim*[‖]*, Yuankai Tang*[§]*, Corban G. E. Murphey*[†]*, Taylor S. Teitsworth*[†]*, Seokhyoung Kim*[⊥]*, Hayk Harutyunyan*[*,§]*, and James F. Cahoon*[*,†]

[†]Department of Chemistry, University of North Carolina at Chapel Hill, Chapel Hill, North Carolina 27599, United States

[§]Department of Physics, Emory University, Atlanta, Georgia 30322, United States

[‖]Department of Physics, Chungbuk National University, Cheongju 28644, Republic of Korea

[⊥]Department of Chemistry, Michigan State University, East Lansing, Michigan 48824, United States

*Corresponding Authors

E-mail: hayk.harutyunyan@emory.edu, jfcahoon@unc.edu

Supporting information includes:

Figures S1–S6

Supporting Figures

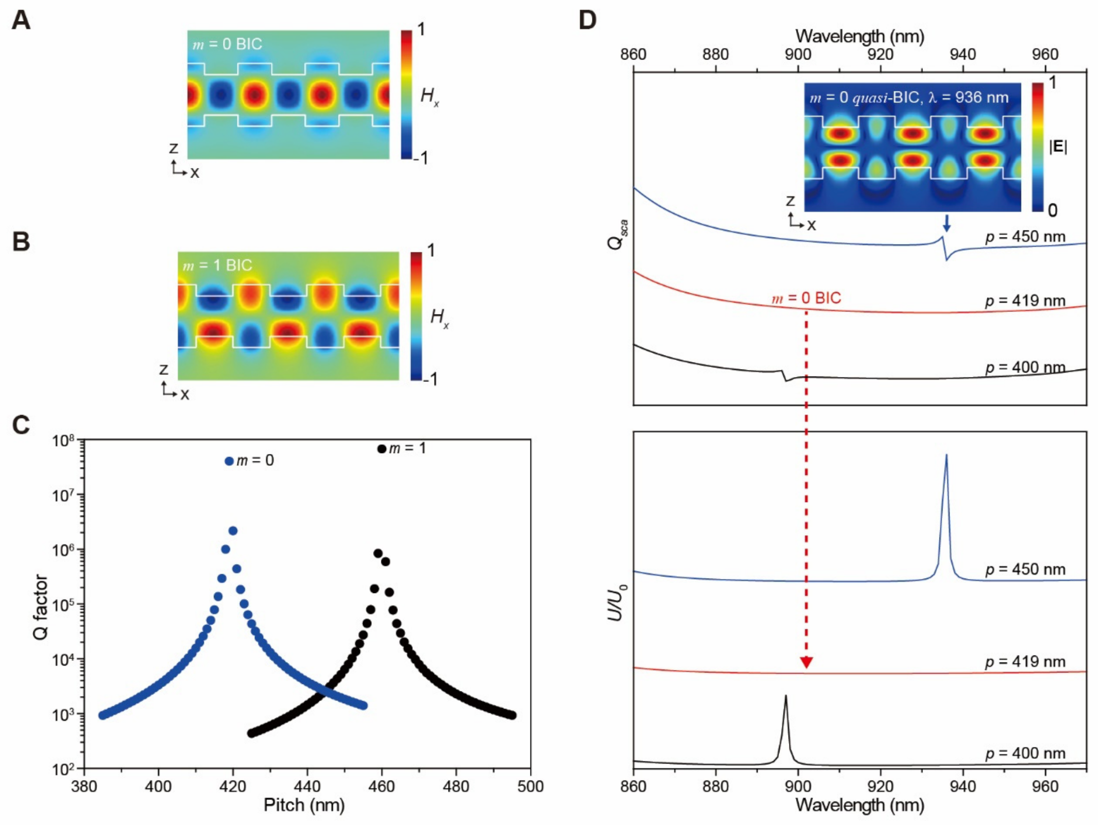

Figure S1. Optical BICs in a Si NW GSL (d = 390 nm; e = 250 nm; $N = \infty$). (**A**,**B**) H_x field distributions calculated from eigenmode analysis for the $m = 0$ BIC with p = 419 nm (panel A) and $m = 1$ BIC with p = 460 nm (panel B). (**C**) Calculated Q factor of Si NW GSL with various p for $m = 0$ (blue dots) and $m = 1$ (black dots). Q factor was obtained without absorptive loss of Si. (**D**) Calculated TE-polarized Q_{sca} (upper panel) and U/U_0 (lower panel) spectra of a Si NW GSL with p = 400 (black), 419 (red), and 450 nm (blue). As p decreases, the Fano features in the Q_{sca} spectra and peaks in U/U_0 spectra associated with $m = 0$ *quasi*-BIC blueshift and disappear at a wavelength of 912 nm with p = 419 nm, the geometry for which the highest Q factor was observed. Inset: calculated |**E**| field distribution resulting from the TE-polarized plane wave scattered by a Si NW GSL with p = 450 nm at the wavelength of 936 nm.

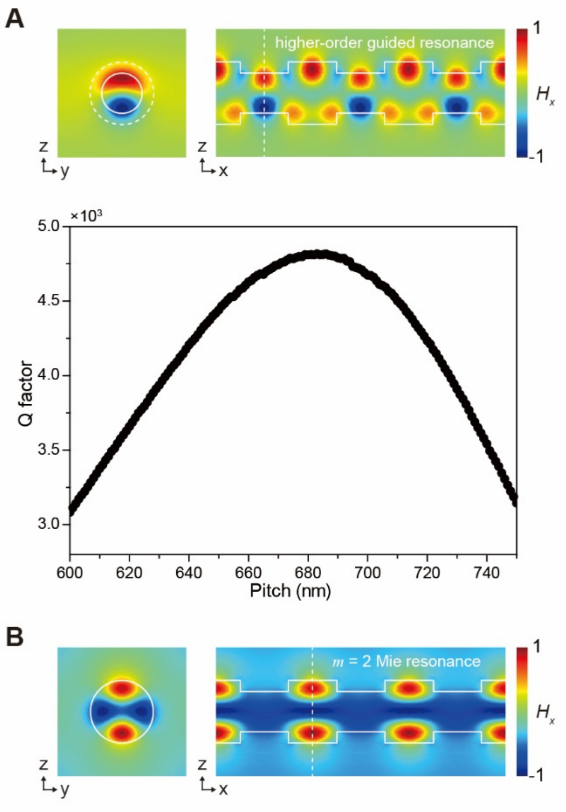

Figure S2. Simulation results for a Si NW GSL with d = 390, e = 250 nm, and $N = \infty$. (**A**) Top: Calculated H_x field distribution of a higher-order guided resonance resulting from the TE-polarized plane wave scattered by a Si NW GSL with p = 600 nm at the wavelength of 889 nm. Both radial cross-sectional (top left panel) and axial cross-sectional (top right panel) H_x field distributions are shown (white dashed line denotes the axial position of the radial cross-section). Bottom: Calculated Q factor of the higher-order guided resonance of Si NW GSLs with various p. Q factor was obtained without absorptive loss of Si. **(B**) Calculated H_x field distribution of the m = 2 Mie resonance resulting from the TE-polarized plane wave scattering by a Si NW GSL with p = 600 nm at the wavelength of 897 nm. Both radial cross-sectional (left) and axial cross-sectional (right) H_x field distributions are shown (white dashed line denotes the axial position of the radial cross-section).

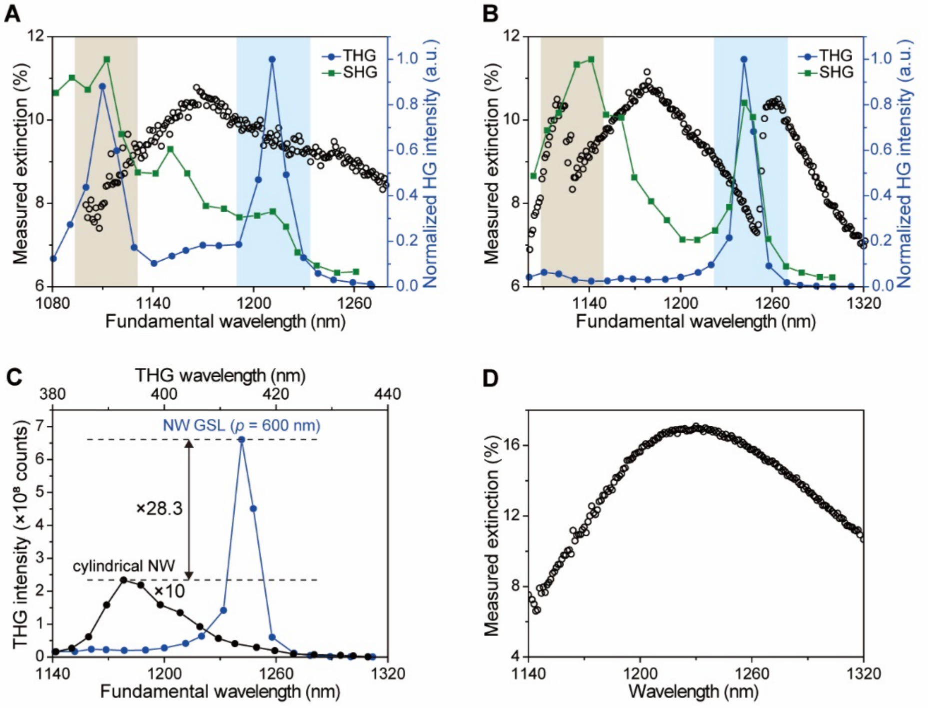

Figure S3. SHG and THG from Si NW GSLs and a cylindrical Si NW. (**A**,**B**) Measured extinction (black open circles), THG intensity (blue closed circles), and SHG intensity (green closed squares) spectra of Si NW GSLs (N = 40) with p = 520 ± 5 nm (panel A) and p = 600 ± 10 nm (panel B). Both THG and SHG intensities are shown normalized to the maximum. Beige and blue colored areas indicate the spectral positions corresponding to the m = 0 and m = 1 *quasi*-BICs, respectively. The extinction and nonlinear measurements were performed using the same Si NW GSL. (**C**) Comparison of THG intensity spectra of the Si NW GSL with p = 600 nm (blue) from panel B and a cylindrical Si NW with d = 410 ± 3 nm (black). The THG spectrum of the cylindrical Si NW has been multiplied by 10 for clarity. The maximal THG intensity measured from the Si NW GSL with p = 600 nm exhibits an ~28.3× enhancement relative to the maximal THG intensity measured with a cylindrical Si NW. (**D**) Measured extinction of a cylindrical Si NW with d = 410 ± 3 nm. Only a broad Mie resonance scattering envelope is observed.

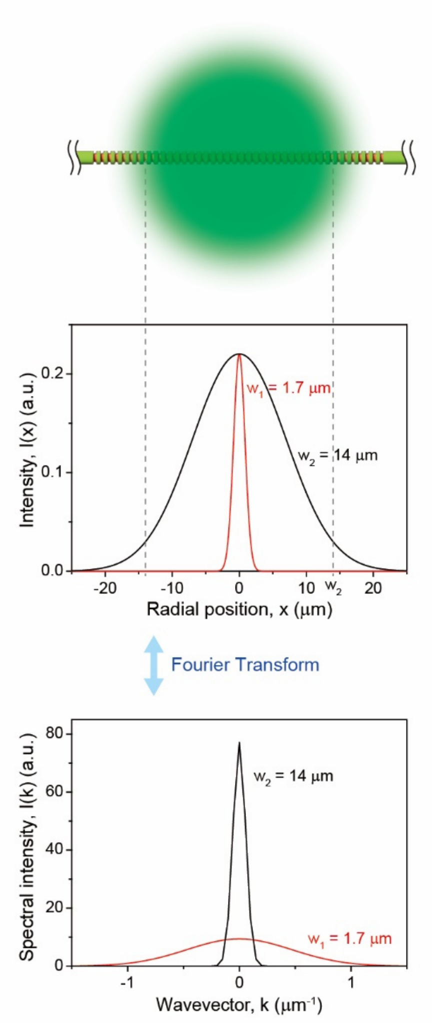

Figure S4. The effect of beam spot on the distribution of the *k*-vectors incident on a GSL. Top: schematic of a Gaussian beam spot and finite-size Si NW GSL with $N = 40$. Middle: intensity profile as a function of radial distance from the center axis of the beam. The Gaussian beam intensity distribution was described by $I(x) = I_0\exp(-2x^2/w^2)$, where I_0, x, and w are the intensity at the center of the beam at its waist, radial distance from the center axis of the beam, and the waist radius, respectively. Two spot sizes of same I_0 were considered depending on the wavelength of the laser light and the numerical aperture (NA) of the objective lens used for nonlinear and extinction measurements. The beam spot used for nonlinear experiments was much smaller than that used for extinction measurements. Bottom: Fourier transformed Gaussian beam intensity in *k*-space. The Gaussian beam of a smaller waist (w_1) shows broader Gaussian distribution in *k*-space compared to the large waist (w_2).

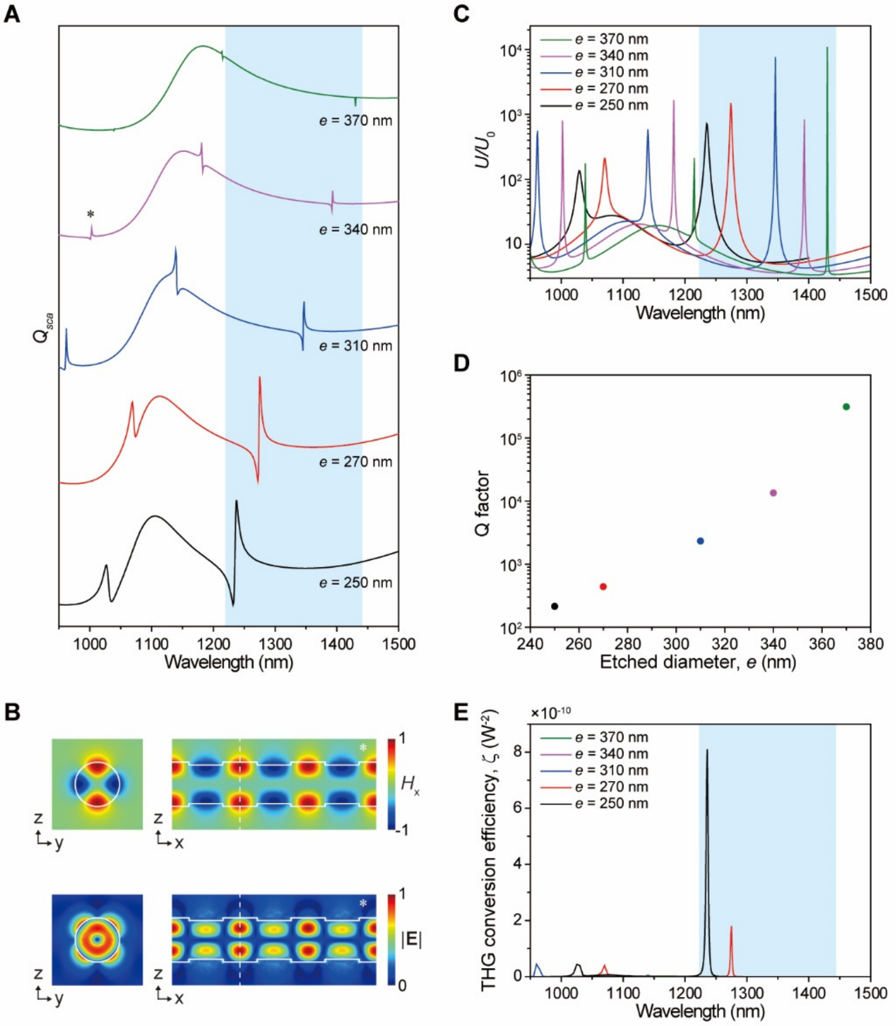

Figure S5. Simulation results for a Si NW GSL with various *e* (*d* = 390 nm and *p* = 600 nm). (**A,C**) Simulated TE-polarized Q_{sca} (panel A) and U/U_0 (panel C) resulting from the TE-polarized plane wave scattered by a Si NW GSL with $N = \infty$. The Fano features at 1029 and 1235 nm are associated with $m = 0$ and 1 quasi-BICs of the Si NW GSL with $e = 250$ nm. As *e* gets closer to *d*, both $m = 0$ and 1 *quasi*-BICs redshift and become sharper. The U/U_0 peaks corresponding to the Fano features in the Q_{sca} spectra show a narrowing linewidth. Blue colored areas indicate the spectral positions corresponding to the $m = 1$ *quasi*-BICs. (**B**) Calculated H_x field (top panel) and |**E**| (bottom panel) distribution of $m = 2$ guided resonance resulting from the TE-polarized plane wave scattered by a Si NW GSL with $e = 340$ nm and $N = \infty$ at the wavelength of 1002 nm, denoted by * in panel A. Both radial cross-sectional (left panel) and axial cross-sectional (right panel) distributions are shown (white dashed line denotes the axial position of the radial cross-section). (**D**) Calculated Q factor of $m = 1$ *quasi*-BICs of Si NW GSLs with various *e*. The increasing Q factor corresponds well to the changes in Q_{sca} and U/U_0 spectra in panel A and C. Q factor was obtained with absorptive loss of Si. (**E**) Simulated THG conversion efficiency (ζ) spectra from Si NW GSLs ($N = 40$). Simulations were performed with the beam spot sizes used in experiments, TE polarization, and $I_0 = 1$ GW/cm^2, which is the intensity at the center of the beam at its waist. The pump power was calculated with $1/2 \times I_0 \pi w^2$, where w is the waist radius. Blue colored areas indicate the spectral positions corresponding to the $m = 1$ *quasi*-BICs. Under experimentally realistic illumination condition, the maximum THG enhancement was observed with $e = 250$ nm, which shows the minimum amplitude of both Q factor and U/U_0.

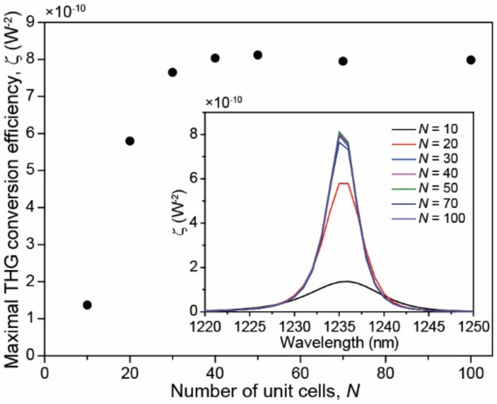

Figure S6. Simulated THG from a finite-size Si NW GSL (*d* = 390 nm; *e* = 250 nm; *p* = 600 nm). The maximal THG conversion efficiency from Si NW GSL as a function of *N*. Inset: simulated THG conversion efficiency (ζ) spectra from Si NW GSLs with various *N*. Simulations were performed with the beam spot sizes used in experiments, TE polarization, and $I_0 = 1$ GW/cm^2, which is the intensity at the center of the beam at its waist. The pump power was calculated with $1/2 \times I_0 \pi \mathrm{w}^2$, where w is the waist radius.